Review of Scientific Instruments

Design and commissioning of the RIKEN cryogenic electrostatic ring (RICE)

Cite as: Rev. Sci. Instrum. **88**, 033110 (2017); https://doi.org/10.1063/1.4978454
Submitted: 22 January 2017 . Accepted: 28 February 2017 . Published Online: 27 March 2017

Y. Nakano, Y. Enomoto, T. Masunaga, S. Menk, P. Bertier, and T. Azuma

View Online Export Citation CrossMark

ARTICLES YOU MAY BE INTERESTED IN

The cryogenic storage ring CSR
Review of Scientific Instruments **87**, 063115 (2016); https://doi.org/10.1063/1.4953888

First storage of ion beams in the Double Electrostatic Ion-Ring Experiment: DESIREE
Review of Scientific Instruments **84**, 055115 (2013); https://doi.org/10.1063/1.4807702

The double electrostatic ion ring experiment: A unique cryogenic electrostatic storage ring for merged ion-beams studies
Review of Scientific Instruments **82**, 065112 (2011); https://doi.org/10.1063/1.3602928



© 2017 Author(s).

Design and commissioning of the RIKEN cryogenic electrostatic ring (RICE)

Y. Nakano,[1,a)] Y. Enomoto,[1] T. Masunaga,[1] S. Menk,[1] P. Bertier,[1,2] and T. Azuma[1,3]
[1]*AMO Physics Laboratory, RIKEN, 351-0198 Saitama, Japan*
[2]*Universite de Lyon, F-69003 Lyon, France; Université Lyon 1, Villeurbanne, France; and CNRS/IN2P3, UMR5822, Institut de Physique Nucléaire de Lyon, F-69622 Villeurbanne, France*
[3]*Department of Physics, Tokyo Metropolitan University, 192-0397 Tokyo, Japan*

(Received 22 January 2017; accepted 28 February 2017; published online 27 March 2017)

A new electrostatic ion storage ring, the RIKEN cryogenic electrostatic ring, has been commissioned with a 15-keV ion beam under cryogenic conditions. The ring was designed with a closed ion beam orbit of about 2.9 m, where the ion beam is guided entirely by electrostatic components. The vacuum chamber of the ring is cooled using a liquid-He-free cooling system to 4.2 K with a temperature difference of 0.4 K at most within all the positions measured by calibrated silicon diode sensors. The first cryogenic operation with a 15-keV Ne^+ beam was successfully performed in August 2014. During the measurement, the Ne^+ beam was stored under a ring temperature of 4.2 K with a residual-gas lifetime of more than 10 min. This permits an estimation of the residual gas density at a few 10^4 cm^{-3}, which corresponds to a room-temperature-equivalent pressure of around 1×10^{-10} Pa. An effect of longitudinal pulse compression at the bunching cavity in the ring was clearly identified by monitoring the pick-up beam detector. The detailed design and mechanical structure of the storage ring, as well as the results from the commissioning run, are reported. *Published by AIP Publishing.* [http://dx.doi.org/10.1063/1.4978454]

I. INTRODUCTION

Storage rings have served as powerful instruments in the high-energy atomic, nuclear, and particle physics fields since the early days of accelerator technology. In addition to the accumulation, acceleration, and deceleration of ion beams, they offer a variety of applications, such as phase-space cooling of the beam, mass analysis, high-luminosity collision, synchrotron radiation emission, and even molecular dynamics studies. The possibility of conducting a molecular physics experiment in a storage ring was first demonstrated in the Test Storage Ring (TSR) at the Max-Planck Institute for Nuclear Physics.[1,2] This triggered many studies on molecular recombination processes performed with respect to molecular structure and reaction dynamics at TARN II (Tokyo),[3] ASTRID (Aarhus),[4] and CRYRING (Stockholm).[5] In 1997, a novel type of storage ring, ELISA, was proposed and built at Aarhus University.[6] In contrast to conventional storage rings with magnetic bending and focusing elements, ELISA achieved beam storage entirely through electrostatic fields. Because electrostatic fields have no mass dispersion, required voltage setting of the ring is independent of ion masses as long as they have the same beam energy per charge. This unique feature of the electrostatic ring offered a new opportunity for storage-ring-based studies of molecules at high-mass regions far beyond the capability of the previous magnetic storage rings. Another advantage of using electrostatic components rather than magnets is that the ring may be compact and less costly, allowing it to be a laboratory-scale device. This prompted developments of similar devices by many experimental groups, as listed in Table I. Taking unique advantage of each device and of rapid progress in developments of instrumentation, experimental studies with stored molecular beams are ongoing with an enormously wide range of interests from basic molecular science to astrochemistry and molecular biology.

The compact size of the electrostatic storage ring has allowed us to vary the temperature of the whole device, similarly to the common manner in ion-trap experiments. The first example of a storage-ring experiment with variable environmental temperatures was performed with ELISA at 220–300 K. The long-debated metastable lifetime of He^- was precisely measured by reducing the effect of blackbody-induced photodetachment of stored ions.[19] After this, a dedicated cold ring, TMU E-ring, was built at the Tokyo Metropolitan University. It has a liquid-nitrogen cooling system inside the vacuum chamber. The effect of cooling was demonstrated in the dependence of the blackbody-induced electron detachment rate of the metastable C^- ions on the ring temperature.[20]

At the beginning of 2010s, construction began on new-generation ultra-cold electrostatic storage rings at Stockholm University,[14] the Max-Planck Institute for Nuclear Physics,[16] and RIKEN.[18] The common principle of these devices is to cool the entire vacuum chamber to below 10 K. The absence of thermal blackbody radiation from the environment offers a unique opportunity to study the dynamics and structure of molecular ions in their vibrational and rotational ground states. In addition, the cryogenic surface of the chamber provides an extremely high vacuum,[21] enabling a long-period storage of ions in the ring.

a)nakano-y@riken.jp

TABLE I. List of electrostatic storage rings for atomic and molecular physics experiments with their location, year of the first publication on stored beam experiments, the nominal temperature T, the nominal maximum beam energy E, and the closed orbit length L of the ring.

Name	Location	Year	T (K)	E (keV)	L (m)
ELISA[6]	Aarhus	1998	300	25	7.6
ES-ring[7]	Tsukuba	2002	300	30	8.1
TMU E-ring[8]	TMU	2007	77–300	30	7.7
Mini-ring[9]	Lyon	2008	300	4	0.73
FLSR[10]	Frankfurt		300	50	14
SAPHIRA[11,12]	Aarhus	2015	300	4	3.9
ELASR[13]	KACST		220–300	30	9.2
DESIREE[14,15]	Stockholm	2013	4–300	25, 100	8.8
CSR[16,17]	MPI-K	2016	4–300	300	35
RICE[18]	RIKEN	2017	4–300	30	2.9

The DESIREE in Stockholm began operation in 2013 and reported the lifetimes of excited levels of atomic anions S^-, Ni^-, and Pt^- over a series of publications.[22–24] Lifetime measurements of long-lived metastable negative ions of up to 500 s became possible for the first time using the cryogenic storage ring. The CSR at the Max-Planck Institute started operation at room temperature in March 2014 and at cryogenic temperature in 2015.[17] They observed the rotational cooling of a CH^+ molecule using the near-threshold photodissociation method.[25] In this report, we will describe the design and technical development of the RIKEN cryogenic electrostatic ring (RICE). Results from the commissioning of the ring with a 15-keV Ne^+ ion beam will also be presented.

II. MECHANICAL DESIGN

A. RICE project overview

In 2011, we began studying the design and construction of a compact cryogenic electrostatic storage ring at RIKEN.[18] The goal of the development of instrumentation was to cool all the electrostatic components and the vacuum chamber to below 5 K with a liquid-He-free cooling system and to attain an extremely high vacuum environment to the order of 10^{-11} Pa. The maximum beam energy is designed to be $30q$ keV, where q is the charge state of the beam. Figure 1 shows an overall view of the RICE facility. The injection beamline was constructed with an electron-cyclotron-resonance (ECR) ion source for commissioning with an intense and stable atomic ion beam. An electrospray ion source (ESI) and a radio frequency (RF) linear ion trap were also installed in the beamline for experiments with molecular and cluster ions. The ion trap is maintained at a cryogenic temperature for the pre-cooling of ions before injection to the ring. These setups allow a variety of complex molecules in a vacuum to be subjected to a laser spectroscopy study with a well-defined quantum state. The beamline has a capacity for further extension towards the right side in Fig. 1 for future upgrade of ion sources.

The cryogenic vacuum chamber of the storage ring is enclosed in a large vacuum tank for thermal isolation from the atmosphere. The chamber is pumped by two pumping chambers connected on the both sides through the four beam ports. The tank is mounted on a linear guide and it can be slid out from the beamline when access to the cryogenic chamber is needed. From above, the storage ring is cooled by three

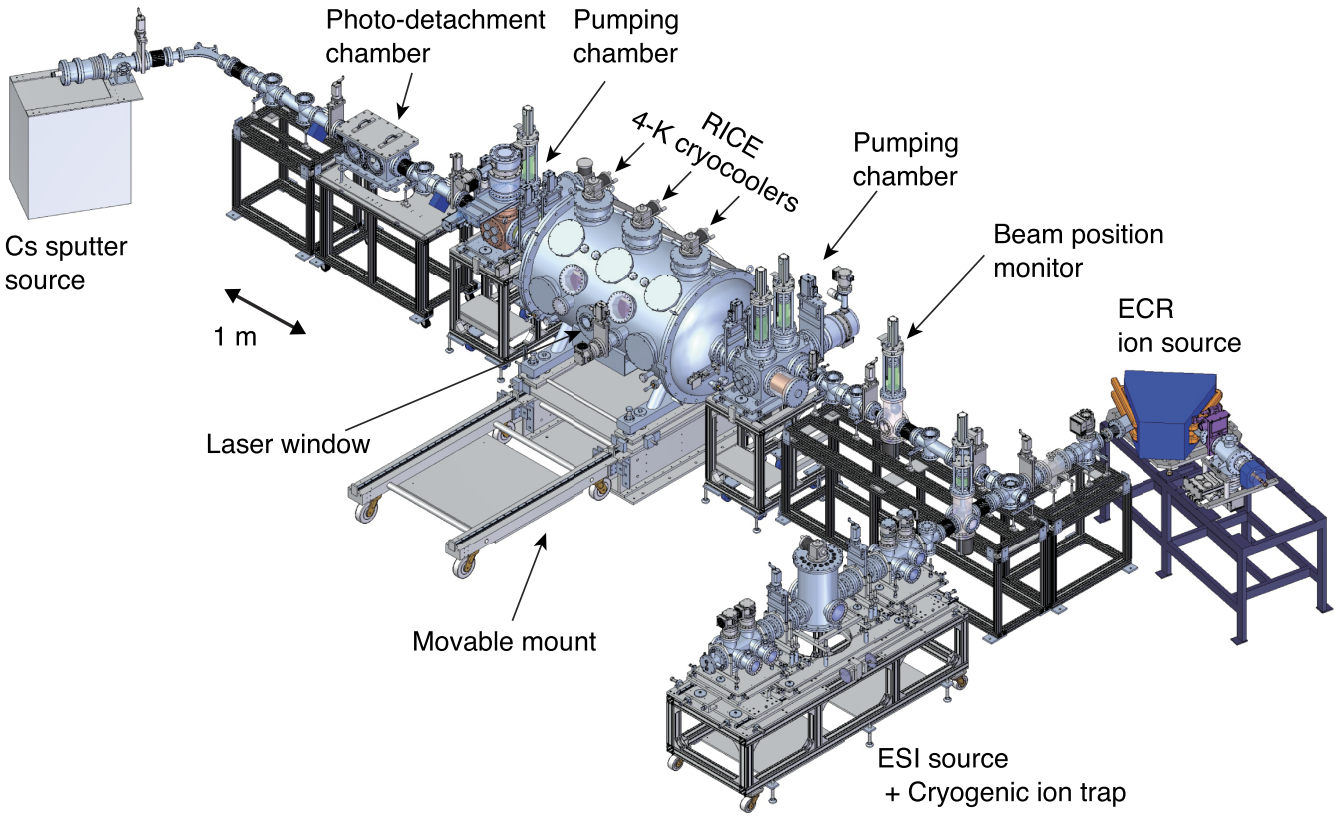


FIG. 1. An overall view of the RICE facility.

cryocoolers that can be easily mounted and dismounted from the chamber using the diagonal maintenance ports of the isolation vacuum tank. A laser window was prepared at the side of vacuum tank in order to perpendicularly irradiate the ion beam in the ring.

From the other side of the ECR and ESI sources, injection of a laser or neutral beam is possible for merged beam experiments. These beams will overlap and cause a high-luminosity collision with the stored ions in the straight section of the ring. An in-ring collinear laser experiment offers high-precision spectroscopy of cold molecules, thanks to the cryogenic ambient temperature and kinematic compression of longitudinal Doppler broadening. Merging with velocity-matched neutral atomic or molecular beams provides a new experimental avenue to study ion-neutral collisions with extremely low center-of-mass energies of less than 10 meV under cryogenic ambient temperatures.

B. Cooling scheme

In this section, we describe the cryogenic technique that allows the RICE to meet the sub-5-K criterion using three two-stage 4 K Gifford-McMahon (GM) cryocoolers. Figure 2 shows a schematic of the RICE cooling system. To eliminate the convection heat load from room-temperature region, the cryogenic chamber and all connecting parts were enclosed in a large vacuum tank with an inner diameter of 1000 mm (JIS 1000 flange) and a length of 1600 mm. The 1st and 2nd stages of the cold head were thermally connected to the radiation shield and the cryogenic chamber, with typical temperatures of 40 K and 4 K, respectively. The radiation shield was made of A1050 aluminum alloy and further covered with multi-layered super insulation sheets to minimize the radiation heat load from ambient room-temperature surfaces into the 4-K region.

Connections to the cold head were made with flexible copper joints in order to absorb the thermal shrinking of the cryogenic parts. This also enables the inner structure to be movable within the isolation vacuum tank, allowing the alignment of the storage ring with respect to the designed beam

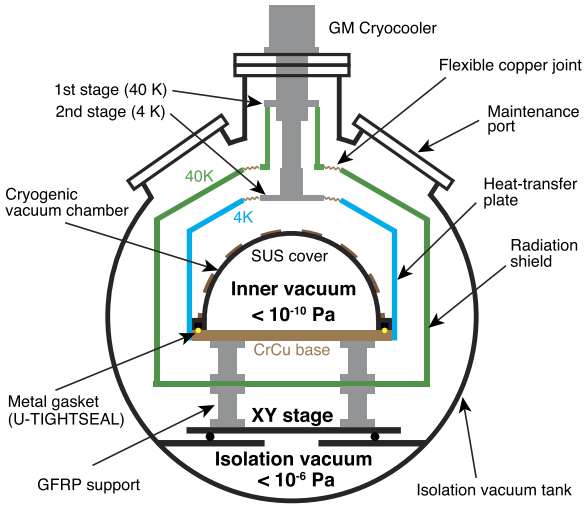


FIG. 2. Schematic cross-sectional view of the RICE structure and cooling system. The 4-K and 40-K regions were covered by multi-layered super insulation sheets which are not shown in the figure.

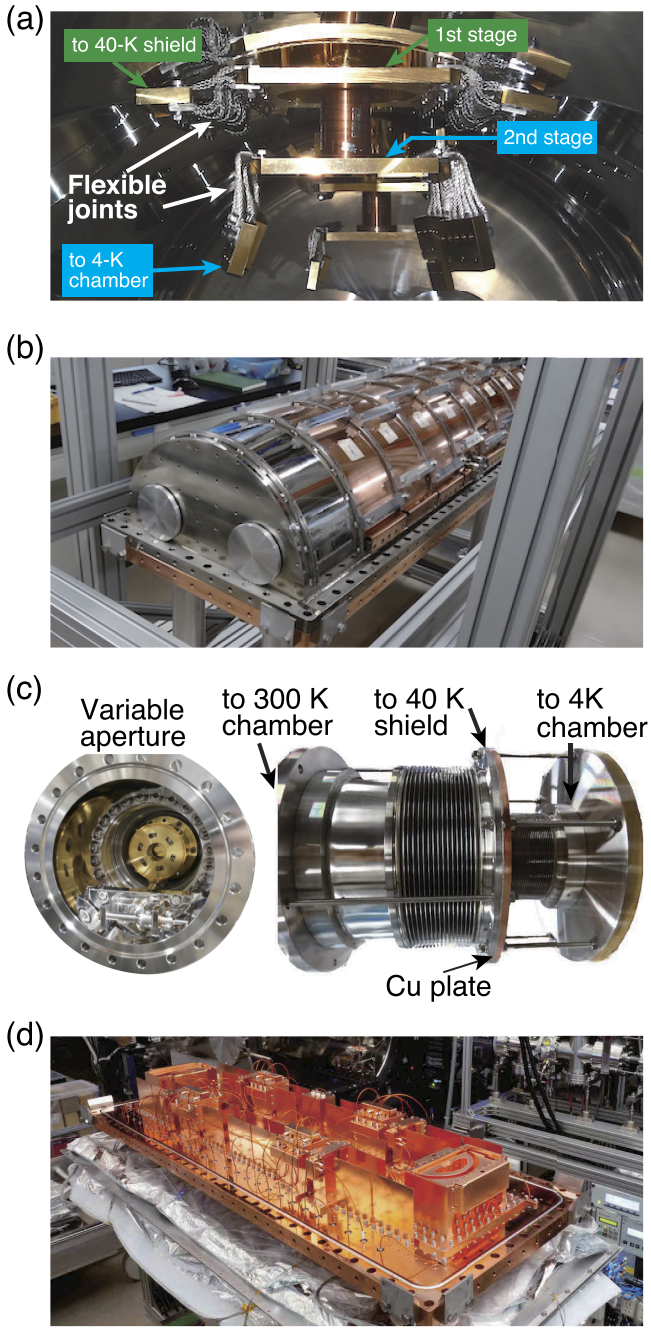


FIG. 3. Photographs of the RICE mechanical structures. (a) One of the cold heads with flexible copper joints installed on the isolation vacuum tank. The copper plates are gold plated to reduce the effective emissivity. (b) The cryogenic chamber made with a CrCu base plate and a SUS304 semi-cylindrical top cover. The heat-conducting OFC plates are attached to the SUS cover. (c) Left: The variable aperture in the beam port seen from the room-temperature side. Right: The beam port possessing two-stage welded bellows with a thermal anchoring flange in the middle. The left- and right-side flanges are connected to the isolation vacuum tank and the cryogenic chamber, respectively. (d) The RICE electrostatic components fixed on the CrCu plate.

axis. Figure 3(a) shows a photograph of the cold head and flexible joints mounted on the top of the isolation tank. The photo was taken from the inside of the tank before installation of the cryogenic chamber and radiation shields. From the 1st and 2nd stages of the cold head, the flexible copper braids are used to hang the gold-plated copper blocks that will be connected to the radiation shield and the cryogenic chamber,

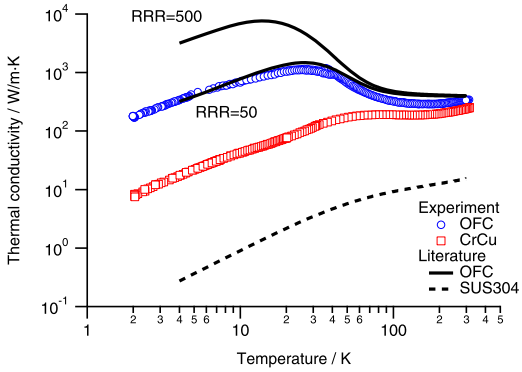


FIG. 4. Temperature dependence of the thermal conductivity of materials used in the RICE. The circle and square show the measured data for OFC and CrCu, respectively. The solid and dashed lines show respectively the thermal conductivity of OFC and SUS304 from the literature.[27] The thermal conductivities of OFC are shown for different purities, i.e., residual resistivity ratios (RRRs) of 50 and 500.

respectively. We made the 2nd-stage flexible joints from braids of 99.9999% (6N) high-purity copper wires because the thermal conductivity of copper dramatically increases with purity at cryogenic temperatures, as shown in Fig. 4. Considering the diameter of the wires, an estimate of the residual resistivity ratio (RRR) of the 6N copper joints reaches a few thousands.[26] Each cryocooler was connected to the chamber via 34 braids in parallel, which have an effective cross-sectional area of 204 mm^2 and a length of 100 mm. On the other hand, the joints for the 1st stage were made from normal oxygen-free copper (OFC) to have an effective area and length of 768 mm^2 and 90 mm at each cooler. The heat-transfer characteristics of the flexible connection were measured with a dedicated test setup in which we measured the temperature difference between both sides of the flexible joint under a variable heat load. The heat resistance associated with the copper joints at each cold head was estimated to be 0.21 and 0.37 K/W for the 1st and 2nd stages, respectively. Note that the heat resistance in the 2nd stage was predominantly created at the contact surfaces, while the resistance of the 6N copper itself is negligibly small. These results were used in the heat load calculation described in detail in Sec. III B.

C. The cryogenic chamber

The mechanical structures of the cryogenic chamber and the connecting parts were designed with full consideration of heat transportation and thermal shrinking. One of the main technical challenges is to realize cooling and sealing of the vacuum chamber simultaneously. Oxygen-free copper (OFC) is commonly used for materials in cryogenic systems, owing to its high thermal conductivity. However, its hardness is not as great as that of stainless steels (SUS) and is not enough to withstand the metal sealing of vacuum chambers. These conflicting requirements were overcome by employing 0.4%–1.0% chromium copper (CrCu) metal alloy. The CrCu alloy combines high thermal conductivity and hardness, and its coefficient for linear thermal expansion is close to those of SUS and OFC. A comparison of the physical properties of the CrCu alloy with those of SUS and OFC is presented in Table II. The CrCu alloy has more than twice the hardness and

TABLE II. Comparison of the thermal and mechanical properties of chromium copper (CrCu), stainless steel (SUS304), and oxygen-free copper (OFC). The coefficient of linear thermal expansion (LTE), yield strength, and Vickers hardness at room temperature are taken from the literature.[28–30]

Property (unit)	CrCu	SUS304	OFC
LTE (10^{-6}/K)	17.6	16	16.6
Yield strength (MPa)	380-490	520	200
Hardness (HV)	135-155	200	51-59

yield strength of OFC, which are around 70%–80% those of SUS304. Because the thermal properties of CrCu at low temperature have not, to our best knowledge, been reported in the literature, we measured the thermal conductivity of CrCu over a temperature range of 2–300 K. Figure 4 shows the results of the measurements for OFC and CrCu used in the RICE, plotted together with the thermal conductivity of SUS304.[27] The thermal conductivities of OFC and CrCu were measured to be 335 and 242 W/(m· K) at 300 K, and 340 and 17 W/(m· K) at 4 K, respectively. Compared to OFC, CrCu alloy exhibited a lower thermal conductivity at 4 K; however, it is still higher than that of SUS304, by more than a factor of 60.

Based on these measurements, we adopted the CrCu alloy as the material for the bottom plate of the cryogenic chamber, with a size of 1674 × 574 mm. The plate has a thickness of 40 mm with a flatness tolerance of 0.5 mm across the area because all the elements of the storage ring will be aligned on it. The CrCu plate is connected to the 2nd stage of the cold heads and acts as a cooling bath for the chamber and internal elements. In terms of reducing the heat capacity, the cover of the chamber was designed to be a thin semi-cylindrical shape (8 mm thick) but strengthened by arching ribs, as shown in Fig. 3(b). Because the cover had to be made from SUS304 as a weldable material, which has a low heat conductivity, OFC plates were attached onto the outer surface of the cover for a better heat transfer. These OFC plates were thermally connected to the CrCu bottom plate after the chamber was closed. This structure is robust against an external pressure of 1 bar, allowing independent pumping of the cryogenic chamber. Distortion by cooling is also negligible because the CrCu and SUS304 have thermal conductivities close to each other, and the residual stress of the SUS cover caused by shaping and welding was removed in advance via a solution heat treatment at 1050 °C. Note that a minor distortion of the SUS cover is anyhow permissible as this does not change the alignment of the ring.

The chamber is sealed at the CrCu–SUS surfaces using a cryo-compatible metal gasket, U-TIGHTSEAL (Usui Kokusai Sangyo Kaisha, Ltd.). The gasket has a C-shaped aluminum jacket with an Inconel spring inside and is pressed by 88 bolts (M16) with a tightening torque of 120 Nm.

The cryogenic chamber is supported from the movable XY stage in the bottom of the isolation vacuum tank (Fig. 2) using five rods made of glass-fiber-reinforced plastics (GFRP). Taking into account thermal shrinking, the chamber and XY stage are rigidly anchored to each other only at their center. The other four rods support the chamber at the corners in a slidable manner using a polytetrafluoroethylene (PTFE)

lubricant sheet. As the XY stage is located in the room-temperature region, the conductive heat load to the chamber must be reduced by designing the GFRP rods with smaller cross-sectional areas and greater lengths. The rods were made to be hollow structures with outer and inner diameters of 60 mm and 40 mm, respectively. In addition, they are separated into upper and lower parts, 60 mm and 110 mm in height, to sandwich the radiation shield in between for thermal anchoring in the middle.

D. Beam ports

The cryogenic chamber has four beam ports for the injection and extraction of the ion beam, as well as of the laser and neutral beams required in the merged-beam experiments. These ports are connected to the room-temperature beamlines and therefore are a significant source of conductive heat load. A photograph of the beam port is shown in Fig. 3(c). They are two-stage welded bellows with a thermal anchor flange in their middle and are made of SUS304. In addition to the low heat conductivity of the SUS304, the small cross sections and long effective length of the bellows play a role in reducing the heat load through them. The middle flange is attached to the OFC plate and connected to the 40-K radiation shield for thermal anchoring. The right- and left-side flanges are connected to the cryogenic chamber and the isolation vacuum tank using the U-TIGHTSEAL and the copper gasket, respectively.

At the thermal anchoring flange of each beam port, a variable aperture is installed, as shown in Fig. 3(c), left. These reduce the room-temperature radiation into the cryogenic chamber as well as to the molecular ions stored in the ring. The aperture is made of six OFC plates forming an iris diaphragm and is controllable by a motorized rotation feedthrough from the outside of the vacuum chamber. The room-temperature side of the apertures is gold plated for high emissivity, and the other side was black-chromium plated to prevent the reflection of radiation into the cryogenic chamber. The opening of the iris is variable from 0 to 25 mm in diameter, and the shutter action can be synchronized with the timing of the injection and extraction of the beam.

E. Electrostatic components

The basic lattice configuration of the storage ring is the same as that of the TMU E-ring,[8] the ES-ring,[7] and ELISA,[6] namely, the beam is bent by two 160° and four 10° deflectors (160DEF and 10DEF) to create a closed orbit and is focused by four sets of electrostatic quadrupole doublet lenses (QF and QD). The sizes of each component are summarized in Table III in comparison with those of the TMU E-ring. The RICE adopted cylindrical deflections for all the 10DEF and 160DEF deflectors in contrast to other rings having parallel-plate-type 10DEFs. The designed circumference of the RICE is L = 2965 mm which has been downsized to be 38% from that of the TMU E-ring. However, the bore size of the straight section of the RICE was kept at 25 mm in order to maintain the high acceptance of the beam.

Figure 3(d) shows a photograph of the electrostatic components of the RICE mounted on the CrCu base plate of the cryogenic chamber. The CrCu base plate is equipped with M6 tapped holes on a 50-mm grid to allow various arrangements of the components. All the electrostatic elements of the storage ring were made from OFC and ceramic insulators and directly screwed to the CrCu plate. As an example, the mechanical structure of the 10DEF is shown in Fig. 5. To maintain high thermal conductivity, the grounded housing of each electrostatic element was machined from a single block of OFC. The high-voltage deflector electrodes were then fixed to the housing using high-thermal-conductivity insulators such as the aluminum nitride (FAN-170, Furukawa Denshi Co., Ltd.) or aluminum oxide (Alumina 96, Hirosugi-Keiki Co., Ltd.). At the right and left sides of the entrance aperture of the deflector, a set of metal plates was installed as a Faraday-plate beam-position monitor. The ion beam current at the Faraday plates were monitored through a charge-sensitive preamplifier or a current amplifier during beam tuning.

TABLE III. Geometric parameters of electrostatic components for the RICE and the TMU E-ring in millimeters. Note that the TMU E-ring adopted parallel-plate deflectors for the 10DEF instead of the cylindrical shape used in the RICE. The length of the 10DEF of the RICE was calculated for its central radius.

Dimensions/mm		RICE	TMU E-ring[8]
Circumference		2965	7736
160DEF	Radius	88.8	250
	Gap	12.15	30
10DEF	Length	(22)	100
	Radius	128.0	...
	Gap	25.0	60
Quadrupoles	Length	38.0	100
	Bore radius	25.0	25

Voltages were applied to the electrodes via coaxial cables connected to the SUS screws using ring-type crimp terminals. To ensure robustness against contact failures and disconnection of the cables, particularly in inaccessible cryogenic regions, two independent cables were wired to each electrode. One is connected to a high voltage power supply, and the other is brought to an 18-bit analog-to-digital converter through a 500:1 voltage divider with a buffer amplifier in order to monitor the electrical potential of the electrodes. All other elements were also designed with the same concept. The voltages to the 10DEFs are applied through high-voltage MOSFET switches (Behlke, HTS61-03-GSM) to enable fast injection and extraction of the beam.

F. Vacuum system

One of the technical goals of the RICE is to attain an extremely low room-temperature-equivalent (RTE) pressure to the order of 10^{-11} Pa. The low temperature of the chamber is essential to increase the condensation pumping speed of the cryogenic surfaces with a total area of about 2 m^2. Therefore, to minimize the heat load, the cryogenic chamber was designed to have no mechanical pumping device or vacuum gauges. Instead, the cryogenic chamber is pumped from

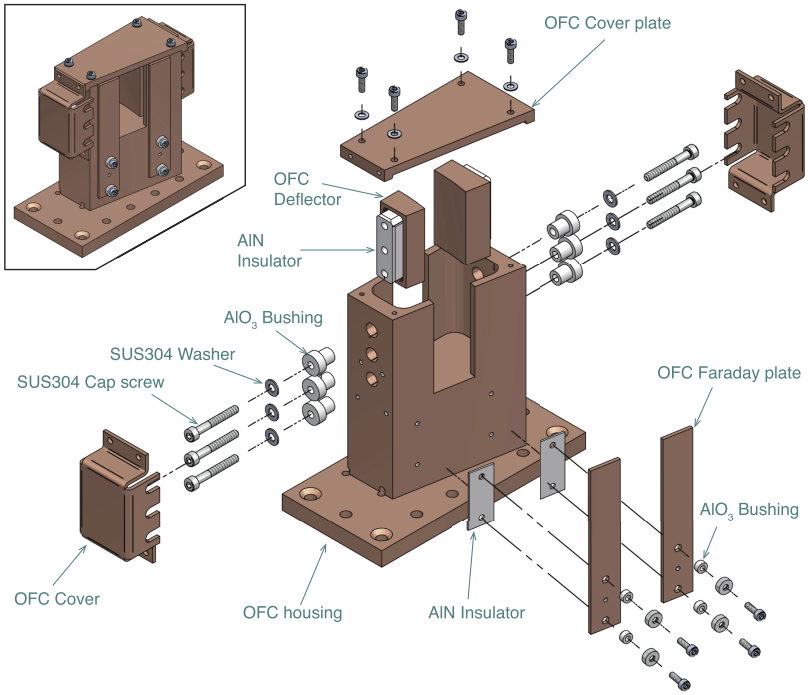


FIG. 5. Structure of the 10° deflector (10DEF) in the RICE.

the room-temperature region through the beam ports. Two pumping chambers were installed at both sides of the ring, as illustrated in Fig. 1, each of which is pumped in tandem by turbo molecular pumps (TG1300MU and TG70F, Osaka Vacuum) backed by an oil-free scroll pump (ISP-250C, Anest Iwata). In an independent pumping test of the pumping chamber after bake out at 250 °C, the pressure was measured to be 2.7×10^{-9} Pa using the extractor vacuum gauges (IE-540, Leybolt).

Although the pressure in the cryogenic chamber cannot be measured directly, expected pressure of the ring P_2 is estimated by $P_2 = P_1 C/S$, where P_1 is the pressure of the pumping chamber, C is the conductance of the beam ports, and S is the pumping speed of the cryogenic chamber. The conductance of the ø25-mm aperture at each beam port is $C = 0.228$ m^3/s. If we assume that the cryogenic surface of the cryogenic chamber has a pumping speed[31] of 1 (m^3/s)/m^2, the expected pressure in the ring is $P_2 = 4 \times 10^{-11}$ Pa. It should be noted that the upper open space in the cryogenic chamber is reserved for additional cryosorption pumping materials, such as the activated charcoal panels to increase the pumping speed for future upgrades.

G. Ion sources

The RICE is currently equipped with two ion sources: a 10-GHz ECR ion source (Nanogan, Pantechnik) on a 20 kV high-voltage bench and an in-house electrospray ionization source (ESI) followed by a cryogenic ion trap and a pulsed 20-keV acceleration. The ECR and ESI sources are installed at different ports of the quadrupole 90° deflector of the beamline, which allows switching of the beam from either source (Fig. 1).

The ECR source produces continuous beams from gaseous atoms or molecules with high intensities up to hundreds of microamperes. The production and transportation of stable beams has been tested with noble gases, as well as hydrocarbons and nitrogen oxides, under optimized source pressure and microwave conditions. The beam extracted from the ECR source is mass-analyzed using a 300-mT dipole magnet and chopped into a pulsed beam for injection to the RICE. The beam chopper comprises a set of adjustable XY slits and a parallel-plate deflector driven by a pulsed high voltage. The detail of beam transport to the ring is described in Sec. IV B.

The ESI source is connected to a quadrupole mass filter, a cryogenic octupole radio frequency (RF) trap, and a pulsed acceleration system (see Fig. 6). In between these elements, the ions are transported by RF octupole ion guides. First, large molecular ions and clusters are produced by the ESI method and passed through a heated capillary. The continuous beam of ions is then mass-selected and accumulated in the ion trap. Helium gas is injected into the trap to slow down the ions and thus keep them trapped. Collisions with the buffer gas also cool the ions' internal degrees of freedom, such as their vibrational and rotational excitation. Since the trap is mounted on a 4 K two-stage GM cryocooler, the helium gas and the trapped ions will be subsequently cooled to cryogenic temperatures.

We also developed a modified trap design that uses a pulsed voltage on additional electrodes between the conventional octupole rods with which the ions can be extracted in a fast and efficient way. This ion bunch is then further accelerated in a pulsed high-voltage tube. The ions enter at low potential, which is then quickly raised while they are drifting in the tube. At the exit side, the ions gain kinetic energies of up to 20 keV with a bunch length on the order of tens of microseconds. Detailed descriptions of the ion trap and the extraction methods will be published elsewhere.

H. Merging beam

The laser and neutral beams were designed to be injected into the RICE and merged with the ion beam stored in the ring. A tunable laser system was constructed in a laser hatch beside

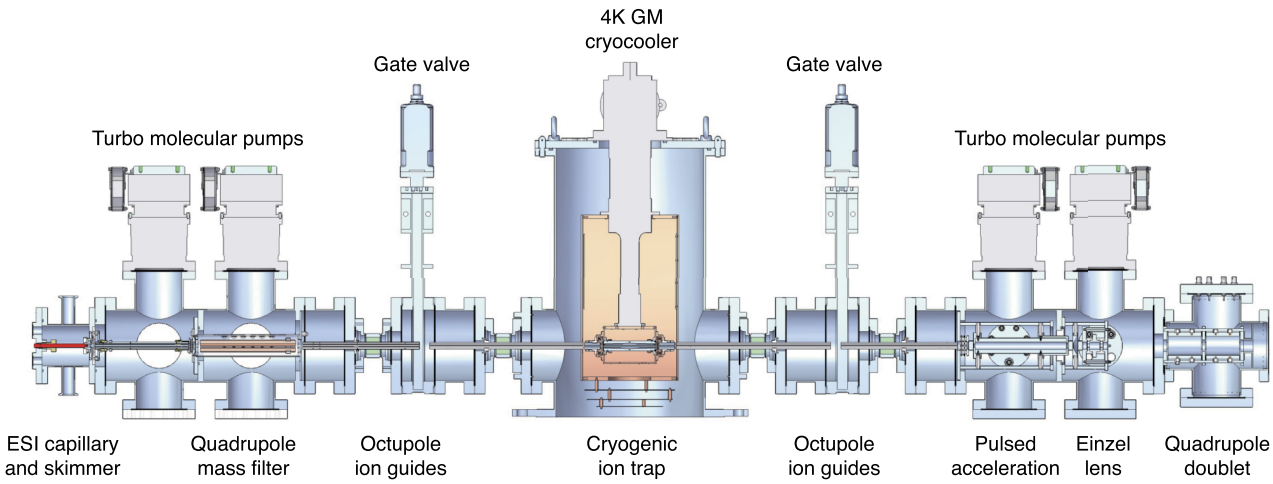


FIG. 6. Cross-sectional view of the cold molecular and cluster ion injection system.

the RICE. Two optical parametric oscillator (OPO) lasers, the Continuum Sunlite EX OPO and the Laser Vision OPO, cover a wide range of wavelengths from 222.5 nm to 5 μm. In addition, for high-resolution spectroscopy, a SIRAH Cobra-Stretch Dye Laser with a tuning range of 370–660 nm was equipped with a frequency-doubling unit. These laser lights enter into the ring through a quartz or sapphire window from one of the beam ports for use in collinear laser experiments. A crossed-beam configuration is also available by using a laser window installed at the side of the chamber. The laser beams are also transported to the cryogenic ion trap setup at the ESI source in order to conduct independent laser experiments in the trap.

Another beamline for a neutral atomic beam was constructed for ion-neutral merging experiments in the RICE. The neutral beam is produced by photo-detachment of a negative ion beam[32] from a Cs-sputter ion source (SNICS II, National Electrostatics Corp.). The negative ion beam is mass-separated by a 500-mT dipole magnet with a bending radius and an angle of 250 mm and 60°, respectively, and transported to the photo-detachment chamber through a movable XY slit and a quadrupole triplet lens. In the photo-detachment chamber, an 808 nm laser diode array shines the beam at a continuous power of 5 kW. The focusing and multi-pass optics of the laser system are currently undergoing testing.

III. NUMERICAL CALCULATIONS

A. Beam optics in the storage ring

The configuration of the electrostatic deflectors and lenses of the RICE is shown in Fig. 7(a). Four beam ports (Ports 1–4) enable injection and extraction of the beam to and from the ring. The stable operation condition of the ring was calculated from the transfer matrix for half a turn in the ring as a unit cell of the lattice. Figure 7(b) shows the stability diagram of the quadrupole voltages calculated for a 15q-keV ion beam. The four shaded areas represent stable voltage conditions of quadrupole lenses, QF and QD, which respectively act as focusing and defocusing elements in the horizontal (X) plane and vice versa in the vertical (Y) plane. The X and Y envelopes of the beam were also calculated along its trajectory s in the ring. Examples are shown in Fig. 7(d) for different voltage conditions, namely, (QF, QD) = (350, 350) and (900, 700) in volts, with the positions and bore sizes of the electrostatic components as filled rectangles.

The origin of the trajectory $s = 0$ corresponds to the center of the straight section. The absolute size of the beam was obtained by assuming the beam emittance in the ring to be 15π mm mrad from the typical value in the TMU E-ring.[33] The beam envelope in two quadrupole conditions displayed different modes of the stored trajectory. A notable difference between the two modes is that the beam is parallel along the straight section when (QF, QD) = (350, 350) V. This condition is favorable in merged-beam experiments because the angular distribution of the beam in the merging region is smaller. On the other hand, when (QF, QD) = (900, 770) V, the beam is focused around $s = 0$ in both X and Y directions. In the crossed-beam configuration, collision luminosity can be efficiently increased at $s = 0$; however, the intra-beam collision may reduce the number of stored ions in the ring.

In the practical design of the shape and structure of the electrostatic elements, we used `SIMION 8.0` to simulate the electrostatic potential and the beam trajectory in each element. Taking into account the effect of fringing fields, we carefully optimized the edge shape and grounded shielding of the electrodes so that they would work as designed in the lattice calculations. An example of the simulated beam trajectory in the ring is traced in Fig. 7(a). The simulation used a 15-keV beam with a spatially uniform distribution over the diameter of 10 mm at Port 1. The beam trajectories were calculated until the beam hit the wall or achieved 2000 turns in the ring. In Fig. 7(c), the average number of ion turns in the simulation is shown as a function of the quadrupole voltages QF and QD. The overall shape of the diagram showed an excellent agreement with the stability diagram calculated using the transfer matrix calculation. This demonstrated that the beam is correctly bent and focused at each element as designed. The trajectory simulation by `SIMION` showed higher probabilities of entering the stable orbits under the lower QF and

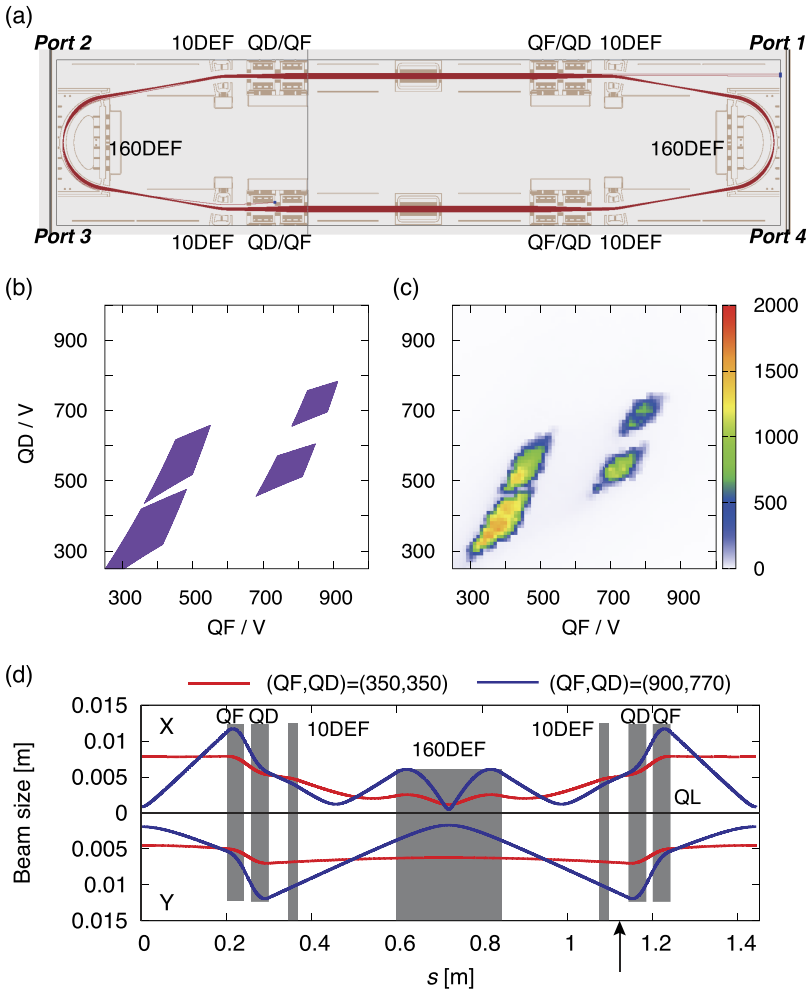


FIG. 7. (a) Layout of the electrostatic components of the RICE, composed of 160° and 10° cylindrical deflectors (160DEF and 10DEF) and quadrupole doublet lens (QD and QF). The chamber has four beam ports for beam injection and extraction. The result of the beam trajectory simulation using SIMION 8.0 is shown by the red trace. (b) Stable operation diagram of the QD and QF voltages for 15-keV beam energy obtained from the transfer matrix calculation. (c) The same stability diagram but simulated using SIMION 8.0 with a ø10-mm parallel beam. The color shows the average number of ion revolutions in the ring calculated up to 2000 turns. (d) The horizontal (X) and vertical (Y) beam envelopes in the RICE calculated for different QD and QF voltages.

QD voltages. There are two reasons for this tendency. One is the maximum size of the beam in the ring, which is generally larger under strong focusing and defocusing conditions. The transfer matrix calculation in Fig. 7(d) clearly demonstrates that the maximum beam size is larger under the higher QF and QD voltages. The other is related to the phase-space matching of the beam at the injection. The incident beam profile used in the simulation was parallel in both X and Y directions. This matches to the stable beam trajectory calculated for (QF, QD) = (350, 350) V; both X and Y beam envelopes are parallel at the position of injection, that is, the entrance of the quadrupole double before the straight section, as indicated by an arrow in Fig. 7(d). Note that the actual position of the injection corresponds to the entrance of the 10DEF; however, the deflector is switched off during the beam injection. On the other hand, under (QF, QD) = (900, 770) V, the stable mode of the beam is divergent in both X and Y directions at the injection position. This leads to the small acceptance of the incident beam into stable orbits under the higher QF and QD voltages.

B. Heat load consideration

The necessary cooling power for the RICE was estimated from the heat load to the cryogenic system. Because there is no internal heat generation from electrostatic elements of the ring, only the heat loads from the room-temperature region must be considered. The radiative and conductive heat loads, Q_R and Q_C, were estimated using the following equations:

$$Q_R = \sigma \epsilon A_R (T_2^4 - T_1^4), \tag{1}$$

$$Q_C = (A_C/L_C) \cdot \int_{T_1}^{T_2} \lambda(T) dT, \tag{2}$$

where σ is the Stefan–Boltzmann constant, A_R is the surface area exposed to the radiation, ϵ is the effective emissivity, and T_1 and T_2 are the temperatures of the higher and lower parts, respectively. The effective emissivity for the super insulator was empirically assumed to be 0.01. For the conductive heat load, A_C and L_C are the cross-sectional area and length of the conductor, and $\lambda(T)$ is the heat conductivity of the material. The estimated Q_R and Q_C to the 1st and 2nd stages of the cooling system are listed in Table IV. The dominant heat loads to the 1st stage are the ambient room-temperature blackbody radiation and the conductive heat flow from the GFRP support. For both the 1st and 2nd stages, the conductive heat load through the beam port is substantially lower than the radiative heat. This indicates that the welded bellows of the beam port contributed significantly to the thermal isolation of the conductive heat.

The heat load to the 1st stage is evaluated to be thirty times larger than that to the 2nd stage. In other words, the heat load from the room-temperature region is well shielded and

TABLE IV. The source and amount of radiative and conductive heat loads, Q_R and Q_C, to the 1st and 2nd stages of the cooling system in watts. The total cooling power of the cryocooler is 120 W at 43 K and 3 W at 4.2 K for the 1st and 2nd stages, respectively.

	1st stage (W)		2nd stage (W)	
Q_R	Vacuum tank	29	40K shield	0.23
	Beam ports	10	Beam ports	0.68
Q_C	Support	19	Support	0.80
	Beam ports	3.8	Beam ports	0.15
	Cables	0.02	Cables	0.19
Total		63		2.1

anchored by the 1st stage in the present design. From these calculations, the GM cryocooler RDK408D2 (Sumitomo Heavy Industries) was chosen as it could provide suitable cooling power distribution into the 1st and 2nd stages. Each cooler has a cooling power of 40 W at 43 K and 1 W at 4.2 K for the 1st and 2nd stages, respectively. The RICE employs a parallel operation of three coolers, with a total cooling power of 120 W and 3 W at the 1st and 2nd stages, respectively, which is sufficiently larger than the total heat load to each stage, as summarized in Table IV.

IV. COMMISSIONING

A. Cooling of the RICE

A test of cooling performance of the RICE was conducted after installation of all the electrostatic components and cables. The ring temperature was monitored by twelve sets of Si diodes and fifteen sets of Pt100 temperature sensors for the 4-K and 40-K regions, respectively. Figure 8 shows the temperature evolutions at different measurement points as a function of time t during the bake out, cooling, and warming procedures. Before the cooling test, the chamber was baked out at 320–325 K using the four sets of 25 Ω ceramic heaters attached onto the CrCu bottom plate. We commenced the cooling process simultaneously with all three cryocoolers at t = 154 h in Fig. 8. Within 160 h after switching on the cooling, the temperature reached thermal equilibrium at 30 K and 3.9 K as measured at the 1st and 2nd stages of the cold heads. The acceleration of cooling observed at around t = 300 h is mainly due to the rapid drop-off of the specific heat of the OFC and SUS in

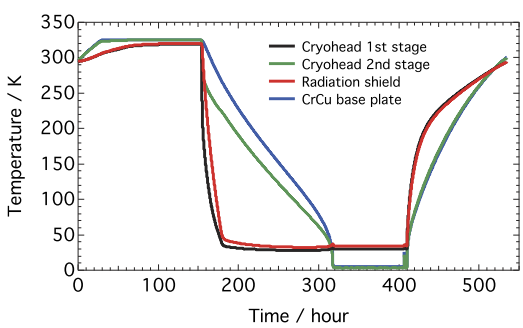


FIG. 8. Temperature of the RICE during the bake out, cooling, and warming procedures.

this temperature region. At equilibrium, the temperature of the chamber was 4.2 K at the CrCu bottom plate and at its highest value, 4.6 K, at the side of the SUS cover where the beam port is connected. At all measurement positions, the chamber temperature attained lower temperatures than the designed value of 5.0 K. Because the temperature difference between the positions within the cryogenic chamber is smaller than 0.5 K, hereafter we refer to the temperature of the CrCu plate as the nominal ring temperature. The temperatures of the radiation shield were between 35 and 40 K. For warming the chamber, the ceramic heaters were operated at a total heating power of 100 W, and the chamber was warmed to 300 K within 130 h. The RICE temperature can be maintained at desired temperatures by regulating the electric current to the ceramic heater via a temperature-feedbacked proportional-integral-derivative (PID) controller.

B. Beam injection and diagnosis

Schematics of the beam injection and diagnosis systems are shown in Fig. 9. Via Ports 1–4, the RICE is connected to the pumping chambers and then to the injection beamline. Using the ECR ion source, beam transport and injection to the RICE were tested with 6.5–20-keV beam energies. The mass-selected beams from the source were focused by an einzel lens to the center of the quadrupole deflector (QDEF) and bent by 90° towards the RICE. The beamline then has an XY slit, a beam steerer (ST), a quadrupole triplet lens (QL1), a quadrupole doublet lens (QL2), and a differential pumping section with three sets of ø10-mm apertures (A1, A2, and A3). The last part of the differential pumping section, the area between A2 and A3, is pumped by two turbo molecular pumps in tandem, and it achieved 7×10^{-8} Pa without bake out.

The beam optics calculation was performed using the analytical beam simulation code `COSY INFINITY`.[34] The parameters for QL1 were set to maximize beam transport efficiency through the set of apertures while those for QL2 were optimized by considering phase space matching at the injection to the ring. An example of the X and Y beam envelopes optimized to the stable beam mode under (QF, QD) = (350, 350) V is shown in Fig. 9. The beam is collimated by QL1 to travel through the apertures and then properly matched by QL2 to the RICE optics. The calculated beam shape in the ring is symmetrical to the storage ring and consistent with the trajectory calculation shown in Fig. 7(d).

Several beam diagnosis systems are installed in the beamline and inside of the RICE. The two-dimensional profile of the beam can be observed using the removable beam profile monitors (BPM) at the beamline (BPM0), the injection port (BPM1), and the extraction ports (BPM2 and BPM4). All the BPMs are installed in room-temperature regions. The BPM consists of a chevron-type ø40-mm micro-channel plate (MCP) assembly and an indium-tin-oxide (ITO)-coated phosphor screen as an anode. The two-dimensional profile at the phosphor screen is online monitored by a CMOS camera externally triggered by a timing signal of the beam. At the same time, the electronic signal from the MCP is simultaneously monitored to observe the total intensity of the beam. Behind

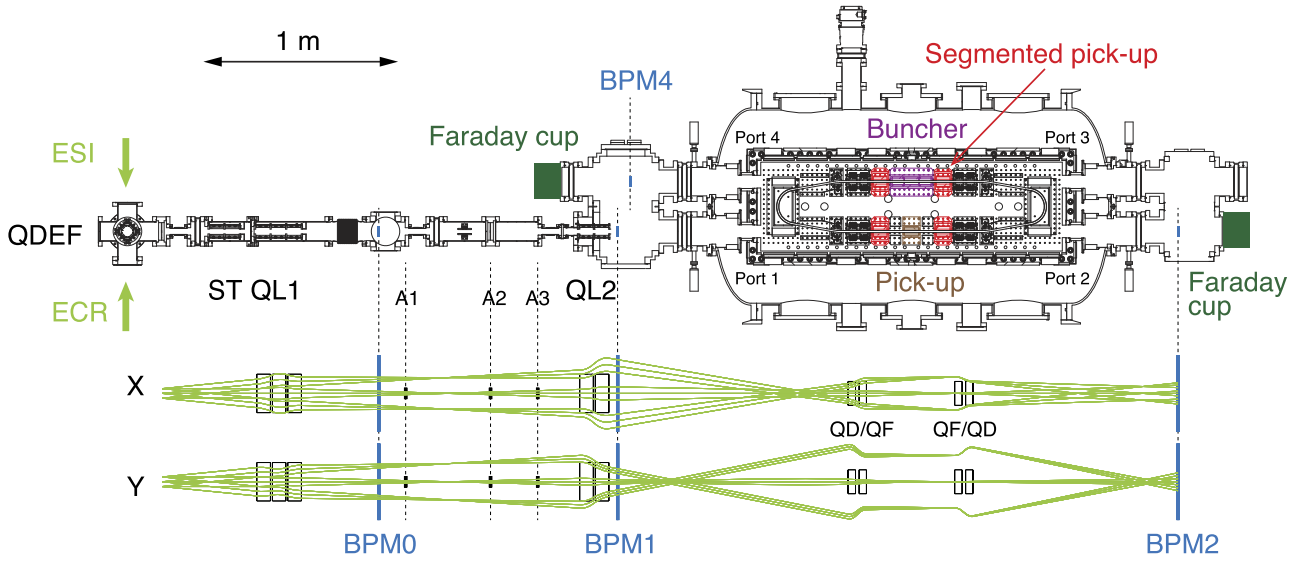


FIG. 9. A schematic view of the RICE injection beamline and diagnosis system. The beamline consists of a 90° quadrupole deflector (QDEF), a beam steerer (ST), a quadrupole triplet lens (QL1), and a quadrupole doublet lens (QL2). Three sets of apertures (A1, A2, and A3) were installed for differential pumping of the beamline. For beam diagnosis, beam profile monitors (BPM), pick-up detectors, and Faraday cups were installed at the indicated locations. An example of the beam optics calculation for the X and Y beam envelopes is also shown with the positions and sizes of the electrostatic elements.

the BPM2 and BPM4, the absolute beam intensity is measurable using a Faraday cup implemented with a charge-sensitive preamplifier.

The beam position in the ring was non-destructively monitored by four pick-up detectors. Each pick-up has a four-segmented cylindrical tube through which the pulsed beam passes. The center-of-mass position of the beam is determined from the relative ratio of the induced-charge signals from the four segments observed through the charge-sensitive preamplifiers. These pick-up detectors were used to tune the conditions of beam injection and storage-ring parameters. In addition to the four position-sensitive pick-up, a non-segmented pick-up detector is also installed at the middle of the straight section in the ring to monitor the beam intensity in the ring. At the other straight section of the RICE, an RF buncher was used to compensate the longitudinal broadening of the beam bunch in the ring, as demonstrated in Sec. IV E.

C. Storage of the 15-keV Ne^+ beam

The first cryogenic operation of the RICE was successfully performed in August 2014 with a 15-keV Ne^+ beam. The Ne^+ beam from the ECR ion source was chopped into 5-μs pulses and injected into the ring by switching off the 10DEF at Port 1 for a short moment during the injection. The revolution frequency of the 15-keV Ne^+ beam in the ring was about 130 kHz. The typical number of ions in the injection beam bunch was 10^6 as measured using the Faraday cup. About 10% of the ions remained in the ring after 1 ms when we extract the beam to the Faraday cup. These ions are considered to be accepted into the stable orbit in the ring. During the storage, the beam intensity in the ring was continuously monitored by counting the number of neutral Ne atoms escaping the orbit due to neutralization of Ne^+ ions in collisions with residual gas in the ring. Figure 10(a) shows the count rate of neutral atoms at BPM4 as a function of time after injection. The confinement time was 18 s over the measurement cycle of 20 s. The data were accumulated for 50 injections, i.e., a measurement time of 1000 s, under different ring temperatures by regulating the ceramic heater installed on the cryogenic chamber of the RICE. For a comparison, a room-temperature measurement with a 20-keV Ne^+ beam[33] in the TMU E-ring is also plotted

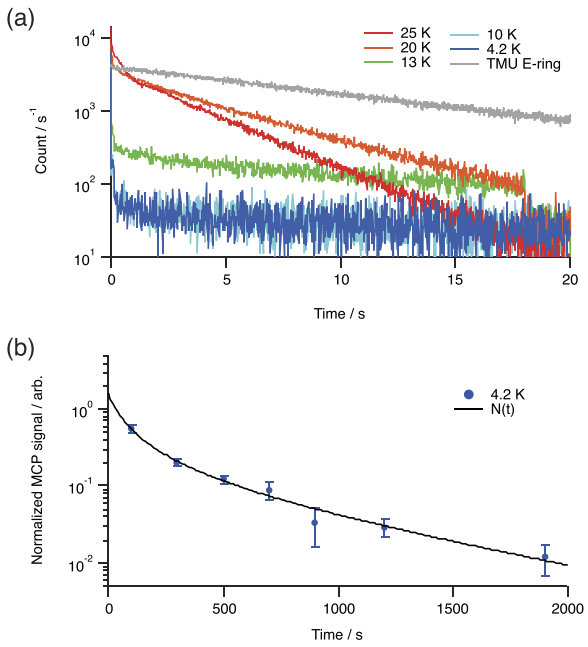


FIG. 10. (a) Neutral counts at BPM4 as a function of time after injection of the 15-keV Ne^+ beam in the RICE. The decay curves were observed under different temperatures at between 4.2 K and 25 K. The time constants of the decay curves were obtained by fitting each curve to an exponential function. For comparison, the same for 20 keV Ne^+ beam in the TMU E-ring[33] measured at room temperature is also shown. (b) The intensity of 15 keV Ne^+ beam at the BPM4 extracted from the RICE at different storage times under temperature of 4.2 K.

in the figure. The TMU data are a sum of 20 injections, and the vacuum gauge of the ring reads 5.14×10^{-9} Pa during the measurement. Note that the geometrical detection efficiencies of the neutral particle may be different for the two rings, although both data are shown in units of count per second.

When the rate of ion loss in the ring is dominated by the interactions with the residual gas, the number of ions in the ring is given by

$$N(t) = N_0 \exp(-t/\tau_{RG}), \tag{3}$$

with a lifetime of

$$\tau_{RG} = 1/(\sigma_{col}\rho v), \tag{4}$$

where σ_{col} is the collision cross section, ρ is the number density of the residual gas, and v is the velocity of the ion beam, respectively. The time constants of the decay curves were obtained by fitting each set of experimental data to the decay function of Eq. (3) in the period of 5 to 18 s. The data points for a storage time of less than 5 s were eliminated in the fitting because the reasons for the rapid decay components observed in this time were not clear. The background count rate of the MCP, that is, the fixed offset for the fitting function, was independently measured without the beam to be 16.4 count/s. The obtained storage lifetime τ_{RG} was 3.05(2) s at 25 K, 4.91(3) s at 20 K, and 17.3(6) s at 13 K. The observations clearly showed that the storage lifetime grows longer with the lowering ring temperature, indicating that the residual gas density ρ in the ring decreases with lowering temperature. At temperatures below 10 K, owing to the extremely low gas density in the ring, the neutral count rate reached the level of the background signal rate. Thus, we were unable to measure the lifetime from the neutral particle detection in the present configuration.

The lifetime of the 15-keV Ne^+ beam at 4.2 K was measured by repeating a destructive observation of the beam intensity at different storage times. The stored beam was dumped onto BPM4 by rapidly switching off the 10DEF at Port4, and the beam current on the MCP was integrated by the charge-sensitive preamplifier. The ion yields measured at different delay times are shown in Fig. 10(b). The observed ion yields were normalized to the initial beam intensity monitored by the pick-up detector and averaged over several injections. The error bars show the standard deviation from the average.

We adopted a model of a decay curve proposed by Reinhed *et al.*[36] The model takes into account the effect of ion loss due to intra-beam ion–ion collisions with a rate proportional to the ion beam intensity and is reported to well explain the experimental data observed in ion-beam trap[36] and storage rings.[14] The time-dependent loss rate $\Gamma(t)$ is described using the loss rate due to residual gas collisions Γ_{RG} and that due to intra-beam collisions $\Gamma_{IB}(t)$, and the number of ions in the ring $N(t)$ is then given by

$$N(t) = \frac{N(0)}{(1+\frac{\Gamma_{IB}(0)}{\Gamma_{RG}})\exp(t\Gamma_{RG}) - \frac{\Gamma_{IB}(0)}{\Gamma_{RG}}}. \tag{5}$$

The fitted curve is shown by a solid line in Fig. 10(b), which gives loss rates of $\Gamma_{RG} = 0.001\,29(37)\ s^{-1}$ and $\Gamma_{IB} = 0.017(14)\ s^{-1}$. Because the rate of intra-beam collision depends on density of ion beams, Γ_{IB} may differ according to the beam mode and intensity in the ring. On the other hand, Γ_{RG} is not affected by the beam condition but determined solely by the residual gas density in the ring. The partial lifetime of the 15-keV Ne^+ beam due to residual gas collisions in the RICE is then $\tau_{RG} = 1/\Gamma_{RG} = 780$ s with an uncertainty of ~35% from the fitting error.

D. Estimation of residual gas density

In this section, we present an estimation of the residual gas density using the measured lifetime in the RICE. The residual gas is approximated by pure H_2 under an extremely high vacuum ($<10^{-8}$ Pa), regardless of its temperature. The residual gas density is related to the loss rate Γ_{RG} in the ring by the following equation:

$$\rho = \Gamma_{RG}/(\sigma_{col}v), \tag{6}$$

where the collisional loss cross section is given by

$$\sigma_{col} = \sigma_{cap} + \sigma_{el}, \tag{7}$$

using the sum of the cross section for electron capture σ_{cap} and that for being elastically scattered out from the ring acceptance σ_{el}. Collisional ionization of the projectile ions is negligible in this energy range. Electron capture cross sections σ_{cap} from the literature are plotted in Fig. 11 for He^+,[35,37–41] Ne^+,[35,37,42] and Ar^+[35,37,43] under the collisions with H_2 molecules. Although the cross section σ_{cap} for Ne^+ in the 10–20 keV energy region is available only from the work of de Heer *et al.*,[35] its consistency can be verified by comparing their cross sections for He^+ and Ar^+ with respect to the data from other literatures.

Elastic scattering cross section σ_{el} is determined by the average amplitude of betatron oscillation of the beam trajectory as well as the inner size of the electrostatic components of the ring. We estimated σ_{el} for a 15-keV Ne^+ beam in the RICE using the experimental data from the TMU E-ring plotted in Fig. 10(a), because both rings were operated under nearly the same condition of beam optics and geometrical configuration of the electrostatic elements. The lifetime of the 20-keV Ne^+ beam in the TMU E-ring was 11.3(4) s under a residual gas density of 2.88×10^6 cm^{-3} as measured by the ionization vacuum gauge. From Eq. (4), the collisional loss cross section σ_{col}

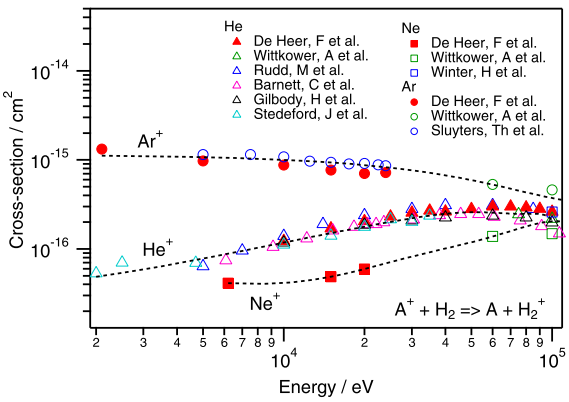


FIG. 11. Electron capture cross sections[35,37–43] for $A^+ + H_2 \rightarrow A + H_2^+$ (where A = He, Ne, Ar) as a function of the collision energy. The data shown by the filled markers are taken from the work of de Heer *et al.*[35] The dashed lines are to guide the eyes.

TABLE V. List of data discussed in the estimation of the residual gas density provided with their experimental conditions and observed storage lifetimes. The cross sections σ_{col}, σ_{cap}, and σ_{el} are given in units 10^{-16} cm^2. The electron capture cross sections σ_{cap} were taken from the literature.[35]

Ring	Beam	ρ (cm^{-3})	τ_{RG} (s)	σ_{col}	σ_{cap}	σ_{el}
TMU E-ring[33]	20 keV Ne$^+$	2.88×10^6	11.3	7.21	0.596	6.62
RICE	15 keV Ne$^+$	2.74×10^4	777	12.3	0.488	11.8
(ES-ring)[7]	20 keV Ne$^+$	2.18×10^6	16.7	6.25	0.596	5.66

is deduced to 7.21×10^{-16} cm^2. Using the electron capture cross section $\sigma_{cap} = 0.596 \times 10^{-16}$ cm^2 from the literature,[35] Eq. (7) gives the elastic collision cross section σ_{el} for the 20-keV Ne$^+$ beam in the TMU E-ring to be 6.62×10^{-16} cm^2, as listed in Table V. The obtained elastic collision cross section σ_{el} was scaled to that for a 15 keV Ne$^+$ beam considering classical Coulomb scattering in which the differential scattering cross section is proportional to the inverse square of the beam energy. This gives $\sigma_{el} = 11.8 \times 10^{-16}$ cm^2, and consequently $\sigma_{col} = 12.3 \times 10^{-16}$ cm^2 for a 15 keV Ne$^+$ beam using the σ_{cap} from the literature. Assuming that the RICE has the same acceptance angle as that of the TMU E-ring, Eq. (6) gives the residual gas density in the RICE at 4.2 K as 2.7×10^4 cm^{-3}. This corresponds to a gas density of 1.3×10^{-10} Pa at room temperature. The uncertainty in this estimation might be as large as a factor of 2; however, we may safely state that the RTE pressure of the RICE at 4.2 K is around 1×10^{-10} Pa. The numerical values used for the estimation are summarized in Table V. The table also lists an estimation of collisional cross section of the 20 keV Ne$^+$ beam of the ES-ring at Tsukuba. Using the reported lifetime and the pressure of the ring,[7] we obtained $\sigma_{el} = 5.66 \times 10^{-16}$ cm^2 which is slightly smaller than that obtained in the TMU E-ring, which is supposed to be due to the difference in the acceptance of the ring.

E. Temporal structure of the stored beam

The temporal structure of the ion bunch in the ring was observed using the non-segmented pick-up detector. Owing to the longitudinal momentum spread of the beam, the bunch length becomes wider and eventually spreads over the entire circumference of the ring. Figure 12(a) shows the pick-up signal from the 15-keV Ne$^+$ ion beam observed at 500 μs, 1 ms, 5 ms, and 10 ms after injection of a 2-μs width ion bunch. The FWHM of the bunch length was 1.5 μs at 500 μs, which spread to 2.4 μs at 5 ms after injection. Assuming that the momentum spread of the beam $\Delta p/p$ is constant over the storage time, the temporal evolution of the bunch structure estimates $\Delta p/p = 4 \times 10^{-4}$ at the FWHM. Considering that the typical energy spread of the ECR source is several electronvolts, the initial momentum spread of the incident beam is on the order of 10^{-4}, which reasonably explains the debunching behavior of the beam. The intra-beam interactions might also contribute to the debunching process at the earlier stage of the storage.

In order to suppress the de-bunching of the beam in the ring, RF bunching was performed during storage. The RF buncher was installed at the straight section of the ring, which consists of three cylindrical tubes as shown in Fig. 12(c). The distance between the two acceleration gaps d is 74 mm, which satisfies $d = L/2h$ with a harmonic number $h = 20$. Figure 12(b) shows the same pick-up signal but with a sinusoidal RF wave applied to the buncher at a frequency of about 2.6 MHz. The RF amplitude was 10 V peak-to-peak, and the frequency was precisely tuned to $f = hv/L$, where the ion revolution frequency v/L was experimentally determined from the spectrum analysis of the pick-up signal. With the RF bunching in the ring, the initial bunch structure was conserved even at 10 ms after injection. This allows beam observation by the pick-up detector for a longer storage period.

The effect of RF bunching is also intelligible in the frequency analysis of the pick up signal. The signal was observed by a spectrum analyzer set to the zero-span mode at the 2nd harmonic of the revolution frequency of the beam. Figure 12(d) shows the signal strength of the 2nd harmonic recorded over the period after the injection. When the RF buncher was switched off, the revolution signal strength decayed to the base level within 10 ms, which is consistent with the time domain observation. On the other hand, with the RF buncher switched on, the decay of the bunch signal strength became significantly slower, such that the signal strength was higher than the background level even after 200 ms.

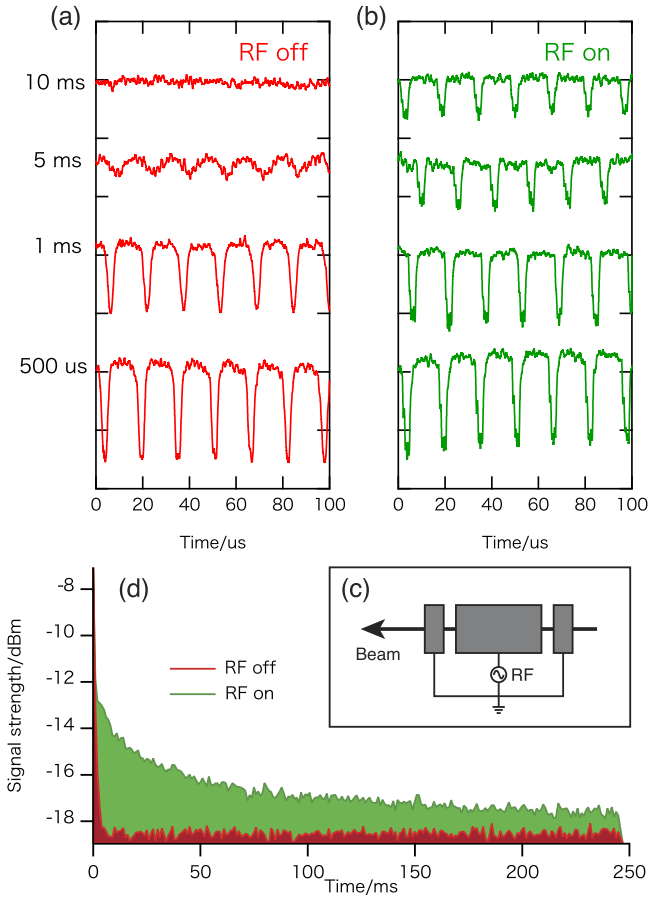


FIG. 12. (a) Pick-up signals from a 15 keV Ne$^+$ beam in the ring. The signal was recorded at 500 μs, 1 ms, 5 ms, and 10 ms after injection. (b) The same but with a 2.6-MHz sine wave applied to the bunching cavity. (c) Schematic structure of the bunching cavity. (d) Strength of the 2nd harmonic of the ion revolution frequency over the period after injection.

V. SUMMARY AND OUTLOOK

The new ion-storage ring RICE was successfully commissioned with a 15-keV Ne^+ ion beam under cryogenic temperatures. The temperature dependence of the storage lifetime clearly showed the reduction of residual gas density in the ring. The lowest temperature of the storage ring attained 4.2 K with a temperature difference of 0.4 K at most over the entire structure of the cryogenic chamber. The use of the CrCu alloy was effective in achieving high heat conductivity and mechanical robustness simultaneously in a vacuum. At this lowest temperature condition, the lifetime of the Ne^+ beam was determined to be about 780 s by using a model of decay curve taking the effect of intra-beam interaction into account. From an analysis of the lifetime using the known cross sections and experimental data from other storage rings, the residual gas density in the RICE was estimated to be approximately 2.7×10^4 cm^{-3}. Considering the uncertainties arising from the fitting and calculation procedures, we conclude that the RTE pressure of the RICE at 4.2 K is around 1×10^{-10} Pa. To upgrade the pumping speed, installation of cryosorption media in the cryogenic chamber is under consideration. In addition, effective operation of the movable aperture at the four beam ports will significantly reduce gas inflow, as well as the radiation heat loads from the room-temperature region.

Several experiments with molecular ions are currently in progress in conjugation with developments of molecular ion sources, neutral beam sources, and the detector systems. Some of the molecular ions from the ECR source have already been tested regarding their injection to the ring and irradiation by tunable lasers for dissociation. Predissociation spectroscopy of these molecular ions is undergoing, aiming to diagnose their internal temperature in the ring. The cryogenic ion trap was also tested with molecular ions from the ESI source. The pulsed acceleration and transportation of the pre-cooled molecular ions are now at a process of optimization. An injection beamline for the neutral beam is under offline testing and will be connected to the other side of the ion injection beamline. Low-energy reactions of the ionic hydrocarbons, hydrogen oxides, and nitrogen oxides with neutral hydrogen, carbon, and oxygen atoms are planned to be investigated in the merging beam experiments.

ACKNOWLEDGMENTS

This work was supported by the RIKEN Basic Science Interdisciplinary Research Projects and by JSPS KAKENHI Grant No. 26220607. Y.N. acknowledges the financial support from JSPS KAKENHI (Nos. 23740311, 26287141, and 16K13859). Y.E. is supported by the Special Postdoctoral Researchers Program of RIKEN. The authors are grateful to S. Jinno for providing the experimental data of Ne^+ measured in the TMU E-ring. The thermal conductivity measurement was performed at the Cryogenic Research Center of the University of Tokyo.

[1]P. Forck, M. Grieser, D. Habs, A. Lampert, R. Repnow, D. Schwalm, A. Wolf, and D. Zajfman, Nucl. Instrum. Methods Phys. Res., Sect. B **79**, 273 (1993).
[2]P. Forck, M. Grieser, D. Habs, A. Lampert, R. Repnow, D. Schwalm, A. Wolf, and D. Zajfman, Phys. Rev. Lett. **70**, 426 (1993).
[3]T. Tanabe, I. Katayama, N. Inoue, K. Chida, Y. Arakaki, T. Watanabe, M. Yoshizawa, S. Ohtani, and K. Noda, Phys. Rev. Lett. **70**, 422 (1993).
[4]L. H. Andersen, J. H. Posthumus, O. Vahtras, H. Ågren, N. Elander, A. Nunez, A. Scrinzi, M. Natiello, and M. Larsson, Phys. Rev. Lett. **71**, 1812 (1993).
[5]M. Larsson, H. Danared, J. R. Mowat, P. Sigray, G. Sundström, L. Broström, A. Filevich, A. Källberg, S. Mannervik, K. G. Rensfelt, and S. Datz, Phys. Rev. Lett. **70**, 430 (1993).
[6]S. P. Møller, Nucl. Instrum. Methods Phys. Res., Sect. A **394**, 281 (1997).
[7]T. Tanabe, K. Chida, K. Noda, and I. Watanabe, Nucl. Instrum. Methods Phys. Res., Sect. A **482**, 595 (2002).
[8]S. Jinno, T. Takao, Y. Omata, A. Satou, H. Tanuma, T. Azuma, H. Shiromaru, K. Okuno, N. Kobayashi, and I. Watanabe, Nucl. Instrum. Methods Phys. Res., Sect. A **532**, 477 (2004).
[9]J. Bernard, G. Montagne, R. Brédy, B. Terpend-Ordacière, A. Bourgey, M. Kerleroux, L. Chen, H. T. Schmidt, H. Cederquist, and S. Martin, Rev. Sci. Instrum. **79**, 075109 (2008).
[10]K. Stiebing, V. Alexandrov, R. Dörner, S. Enz, N. Kazarinov, T. Kruppi, A. Schempp, H. Schmidt Böcking, M. Völp, P. Ziel, M. Dworak, and W. Dilfer, Nucl. Instrum. Methods Phys. Res., Sect. A **614**, 10 (2010).
[11]H. B. Pedersen, A. Svendsen, L. S. Harbo, H. V. Kiefer, H. Kjeldsen, L. Lammich, Y. Toker, and L. H. Andersen, Rev. Sci. Instrum. **86**, 063107 (2015).
[12]A. Svendsen, R. Teiwes, H. V. Kiefer, L. H. Andersen, and H. B. Pedersen, Rev. Sci. Instrum. **87**, 013111 (2016).
[13]M. El Ghazaly, S. Alshammari, C. Welsch, and H. Alharbi, Nucl. Instrum. Methods Phys. Res., Sect. A **709**, 76 (2013).
[14]H. T. Schmidt, R. D. Thomas, M. Gatchell, S. Rosén, P. Reinhed, P. Löfgren, L. Brännholm, M. Blom, M. Björkhage, E. Bäckström, J. D. Alexander, S. Leontein, D. Hanstorp, H. Zettergren, L. Liljeby, A. Källberg, A. Simonsson, F. Hellberg, S. Mannervik, M. Larsson, W. D. Geppert, K. G. Rensfelt, H. Danared, A. Paál, M. Masuda, P. Halldén, G. Andler, M. H. Stockett, T. Chen, G. Källersjö, J. Weimer, K. Hansen, H. Hartman, and H. Cederquist, Rev. Sci. Instrum. **84**, 055115 (2013).
[15]R. D. Thomas, H. T. Schmidt, G. Andler, M. Björkhage, M. Blom, L. Brännholm, E. Bäckström, H. Danared, S. Das, N. Haag, P. Halldén, F. Hellberg, A. I. S. Holm, H. A. B. Johansson, A. Källberg, G. Källersjö, M. Larsson, S. Leontein, L. Liljeby, P. Löfgren, B. Malm, S. Mannervik, M. Masuda, D. Misra, A. Orbán, A. Paál, P. Reinhed, K.-G. Rensfelt, S. Rosén, K. Schmidt, F. Seitz, A. Simonsson, J. Weimer, H. Zettergren, and H. Cederquist, Rev. Sci. Instrum. **82**, 065112 (2011).
[16]R. von Hahn, F. Berg, K. Blaum, J. Crespo Lopez-Urrutia, F. Fellenberger, M. Froese, M. Grieser, C. Krantz, K.-U. Kühnel, M. Lange, S. Menk, F. Laux, D. Orlov, R. Repnow, C. Schröter, A. Shornikov, T. Sieber, J. Ullrich, A. Wolf, M. Rappaport, and D. Zajfman, Nucl. Instrum. Methods Phys. Res., Sect. B **269**, 2871 (2011).
[17]R. Von Hahn, A. Becker, F. Berg, K. Blaum, C. Breitenfeldt, H. Fadil, F. Fellenberger, M. Froese, S. George, J. Göck, M. Grieser, F. Grussie, E. A. Guerin, O. Heber, P. Herwig, J. Karthein, C. Krantz, H. Kreckel, M. Lange, F. Laux, S. Lohmann, S. Menk, C. Meyer, P. M. Mishra, O. Novotný, A. P. O'Connor, D. A. Orlov, M. L. Rappaport, R. Repnow, S. Saurabh, S. Schippers, C. D. Schröter, D. Schwalm, L. Schweikhard, T. Sieber, A. Shornikov, K. Spruck, S. Sunil Kumar, J. Ullrich, X. Urbain, S. Vogel, P. Wilhelm, A. Wolf, and D. Zajfman, Rev. Sci. Instrum. **87**, 063115 (2016).
[18]Y. Nakano, W. Morimoto, T. Majima, J. Matsumoto, H. Tanuma, H. Shiromaru, and T. Azuma, J. Phys.: Conf. Ser. **388**, 142027 (2012).
[19]U. V. Pedersen, M. Hyde, S. P. Møller, and T. Andersen, Phys. Rev. A **64**, 012503 (2001).
[20]T. Takao, S. Jinno, K. Hanada, M. Goto, K. Oshikiri, K. Okuno, H. Tanuma, T. Azuma, and H. Shiromaru, J. Phys.: Conf. Ser. **88**, 012044 (2007).
[21]M. Lange, M. Froese, S. Menk, J. Varju, R. Bastert, K. Blaum, J. R. C. Lopez-Urrutia, F. Fellenberger, M. Grieser, R. von Hahn, O. Heber, K.-U. Kuhnel, F. Laux, D. A. Orlov, M. L. Rappaport, R. Repnow, C. D. Schroter, D. Schwalm, A. Shornikov, T. Sieber, Y. Toker, J. Ullrich, A. Wolf, and D. Zajfman, Rev. Sci. Instrum. **81**, 055105 (2010).
[22]E. Bäckström, D. Hanstorp, O. M. Hole, M. Kaminska, R. F. Nascimento, M. Blom, M. Björkhage, A. Källberg, P. Löfgren, P. Reinhed, S. Rosén, A. Simonsson, R. D. Thomas, S. Mannervik, H. T. Schmidt, and H. Cederquist, Phys. Rev. Lett. **114**, 143003 (2015).
[23]K. C. Chartkunchand, M. Kamińska, E. K. Anderson, M. K. Kristiansson, G. Eklund, O. M. Hole, R. F. Nascimento, M. Blom, M. Björkhage, A. Källberg, P. Löfgren, P. Reinhed, S. Rosén, A. Simonsson, R. D. Thomas, S. Mannervik, V. T. Davis, P. A. Neill, J. S. Thompson, D. Hanstorp,

H. Zettergren, H. Cederquist, and H. T. Schmidt, Phys. Rev. A **94**, 032501 (2016).
[24]M. Kamińska, V. T. Davis, O. M. Hole, R. F. Nascimento, K. C. Chartkunchand, M. Blom, M. Björkhage, A. Källberg, P. Löfgren, P. Reinhed, S. Rosén, A. Simonsson, R. D. Thomas, S. Mannervik, P. A. Neill, J. S. Thompson, H. T. Schmidt, H. Cederquist, and D. Hanstorp, Phys. Rev. A **93**(1), 012512 (2016).
[25]A. O'Connor, A. Becker, K. Blaum, C. Breitenfeldt, S. George, J. Göck, M. Grieser, F. Grussie, E. Guerin, R. von Hahn, U. Hechtfischer, P. Herwig, J. Karthein, C. Krantz, H. Kreckel, S. Lohmann, C. Meyer, P. Mishra, O. Novotný, R. Repnow, S. Saurabh, D. Schwalm, K. Spruck, S. Sunil Kumar, S. Vogel, and A. Wolf, Phys. Rev. Lett. **116**, 113002 (2016).
[26]K. Mimura, Y. Ishikawa, M. Isshiki, and M. Kato, Mater. Trans., JIM **38**, 714 (1997).
[27]E. D. Marquardt, J. P. Le, and R. Radebaugh, *Cryocoolers 11* (Kluwer Academic Publishers, Boston, 2001), pp. 681–687.
[28]J. Ekin, *Experimental Techniques for Low-temperature Measurements: Cryostat Design, Material Properties and Superconductor Critical-current Testing* (Oxford University Press, 2006).
[29]Japanese Standards Association, *JIS Handbook Ferrous Materials and Metallurgy I* (Japanese Standards Association, 2016).
[30]Japanese Standards Association, *JIS Handbook Non-ferrous Metals and Metallurgy* (Japanese Standards Association, 2016).
[31]G. F. Weston, *Ultrahigh Vacuum Practice* (Butterworths, 1985).
[32]A. P. O'Connor, F. Grussie, H. Bruhns, N. de Ruette, T. P. Koenning, K. A. Miller, D. W. Savin, J. Stützel, X. Urbain, and H. Kreckel, Rev. Sci. Instrum. **86**, 113306 (2015).
[33]S. Jinno, "Storage of atomic/molecular ions in an electrostatic ring," Ph.D. thesis, Tokyo Metropolitan University, 2007.
[34]K. Makino and M. Berz, Nucl. Instrum. Methods Phys. Res., Sect. A **558**, 346 (2006).
[35]F. De Heer, W. Huizenga, and J. Kistemaker, Physica **23**, 181 (1957).
[36]P. Reinhed, A. Orbán, S. Rosén, R. Thomas, I. Kashperka, H. Johansson, D. Misra, A. Fardi, L. Brännholm, M. Björkhage, H. Cederquist, and H. Schmidt, Nucl. Instrum. Methods Phys. Res., Sect. A **621**, 83 (2010).
[37]A. B. Wittkower and H. B. Gilbody, Proc. Phys. Soc. **90**, 353 (1967).
[38]M. E. Rudd, T. V. Goffe, A. Itoh, and R. D. DuBois, Phys. Rev. A **32**, 829 (1985).
[39]C. F. Barnett and H. K. Reynolds, Phys. Rev. **109**, 355 (1958).
[40]H. B. Gilbody, K. F. Dunn, R. Browning, and C. J. Latimer, J. Phys. B: At. Mol. Phys. **4**, 800 (1971).
[41]J. B. H. Stedeford and J. B. Hasted, Proc. R. Soc. A **227**, 466 (1955).
[42]H. Winter, E. Bloemen, and F. J. der Heer, J. Phys. B: At. Mol. Phys. **10**, L453 (1977).
[43]T. Sluyters, E. De Haas, and J. Kistemaker, Physica **25**, 1376 (1959).